

Electronic Structure of Transition-Metal Dicyanamides $\text{Me}[\text{N}(\text{CN})_2]_2$ (Me = Mn, Fe, Co, Ni, Cu)

D. O. Demchenko and Amy Y. Liu

Department of Physics, Georgetown University, Washington, DC 20057, USA

E. Z. Kurmaev, L. D. Finkelstein and V. R. Galakhov

Institute of Metal Physics, Russian Academy of Sciences-Ural Division, 620219 Yekaterinburg GSP-170, Russia

A. Moewes

*Department of Physics and Engineering Physics, University of Saskatchewan,
116 Science Place, Saskatoon, Saskatchewan S7N 5E2, Canada*

S. G. Chiuzbăian* and M. Neumann

Universität Osnabrück, Fachbereich Physik, D-49069 Osnabrück, Germany

Carmen R. Kmety

Advanced Photon Source, Argonne National Laboratory, Argonne IL 60439, USA

Kenneth L. Stevenson

Department of Chemistry, Indiana University Purdue University, Fort Wayne, Indiana 46805, USA

(Dated: April 12, 2018)

The electronic structure of $\text{Me}[\text{N}(\text{CN})_2]_2$ (Me=Mn, Fe, Co, Ni, Cu) molecular magnets has been investigated using x-ray emission spectroscopy (XES) and x-ray photoelectron spectroscopy (XPS) as well as theoretical density-functional-based methods. Both theory and experiments show that the top of the valence band is dominated by Me 3d bands, while a strong hybridization between C 2p and N 2p states determines the valence band electronic structure away from the top. The 2p contributions from non-equivalent nitrogen sites have been identified using resonant inelastic x-ray scattering spectroscopy with the excitation energy tuned near the N 1s threshold. The binding energy of the Me 3d bands and the hybridization between N 2p and Me 3d states both increase in going across the row from Me = Mn to Me = Cu. Localization of the Cu 3d states also leads to weak screening of Cu 2p and 3s states, which accounts for shifts in the core 2p and 3s spectra of the transition metal atoms. Calculations indicate that the ground-state magnetic ordering, which varies across the series is largely dependent on the occupation of the metal 3d shell and that structural differences in the superexchange pathways for different compounds play a secondary role.

PACS numbers: 75.50.Xx, 71.20.Rv, 71.70.-d, 75.30.Et

I. INTRODUCTION

Molecule-based magnets have been a subject of interest in the past decade, after the discovery of room-temperature magnetic ordering in some of these materials.^{1,2} Interest is driven not only by the potential for use in applications like information storage and processing, but also by fundamental questions about the origin of magnetic ordering in these materials. The transition-metal dicyanamides, $\text{Me}[\text{N}(\text{CN})_2]_2$ where Me is a 3d transition metal, provide an example where, even within an isostructural series of compounds, the magnetic ordering can differ substantially depending on the metal species and details of the crystal structure. Experimental studies of the structural and magnetic properties of the dicyanamides with Me = Mn, Fe, Co, Ni, and Cu have been performed by several groups.^{3,4,5,6,7,8} $\text{Mn}[\text{N}(\text{CN})_2]_2$ and $\text{Fe}[\text{N}(\text{CN})_2]_2$ have been found to be canted antiferromagnets, while $\text{Co}[\text{N}(\text{CN})_2]_2$ and $\text{Ni}[\text{N}(\text{CN})_2]_2$ have been found to be ferromagnets. $\text{Cu}[\text{N}(\text{CN})_2]_2$ has been reported to be paramagnetic, at least down to a few Kelvin, and a recent experiment has found that it becomes a ferromagnet below 1.8 K.⁸ Thus the compounds with transition-metal ions having six or fewer 3d electrons order as canted antiferromagnets, while those with seven or more 3d electrons order as ferromagnets. The Curie (or Néel) temperatures of these materials range from 1.8 K for $\text{Cu}[\text{N}(\text{CN})_2]_2$ to 22.7 K for $\text{Ni}[\text{N}(\text{CN})_2]_2$. $\text{Ni}[\text{N}(\text{CN})_2]_2$ and $\text{Fe}[\text{N}(\text{CN})_2]_2$ have been found to have the largest coercive fields of all known metal-organic magnets – 7975 and 17800 Oe, respectively.

* Present address: Paul Scherrer Institut, Swiss Light Source, CH-5232 Villigen, Switzerland

The molecular building block of the bulk dicyanamides consists of a divalent metal ion that is two-fold coordinated by two $\text{N}(\text{CN})_2$ groups. When the molecular units pack to form the bulk crystal, the negatively charged CN groups at the end of neighboring molecules interact with the positive central metal ion in such a way that the metal ion becomes surrounded by an octahedron of six N atoms. The local symmetry around the metal site is tetragonal, with the original molecular axis corresponding to the long axis. The primitive cell contains two formula units with their long axes rotated in opposite directions in the xy plane, leading to an orthorhombic cell. The metal ions are the source of magnetic moments while the organic species provide superexchange pathways between the magnetic centers.

In this paper, we report a combined experimental and theoretical study of the electronic structure of $\text{Me}[\text{N}(\text{CN})_2]_2$ with $\text{Me} = \text{Mn}, \text{Fe}, \text{Co}, \text{Ni}, \text{Cu}$. We have measured x-ray emission spectra (XES) and x-ray photoemission spectra (XPS) across the series. Generally, XPS probes the total occupied density of states (DOS) whereas XES probes the site-selective partial DOS due to the dipole selection rules. In the case of carbon and nitrogen K_α XES, which correspond to $2p \rightarrow 1s$ transitions, the occupied $2p$ states can be studied. Similarly, Me $L_{2,3}$ XES, related to the $3d4s \rightarrow 2p$ transition, gives information about occupied $3d$ bands. The comparison of XPS and XES in the binding-energy scale yields information about the distribution of the partial and total DOS in multicomponent systems. The measured spectra are compared with results of density-functional calculations. In a recent paper focusing on the electronic structure of $\text{Mn}[\text{N}(\text{CN})_2]_2$, reasonable agreement was found between theory and experiment for the electronic structure, magnetic ordering, and magnetic anisotropy.⁹ Here we find that the direct comparison of density-functional calculations with experimental data is not as straightforward for some of the other compounds in the series.

II. EXPERIMENTAL AND CALCULATION DETAILS

The x-ray fluorescence measurements were performed at Beamline 8.0 at the Advanced Light Source (ALS) of Lawrence Berkeley National Laboratory (LBNL). Carbon and nitrogen K_α ($2p \rightarrow 1s$ transition) and Me $L_{2,3}$ ($3d4s \rightarrow 2p$ transition) x-ray emission spectra were taken, employing the University of Tennessee at Knoxville soft x-ray fluorescence endstation.¹⁰ Photons with energy of 300 eV above the carbon K edge were delivered to the endstation via the beamline's 89-period, 5 centimeter undulator insertion device and spherical monochromator. For nitrogen K_α and Me $L_{2,3}$ XES, an excitation-energy dependence was measured near the N $1s$ and Me $2p$ thresholds. The carbon and nitrogen K_α spectra were obtained with an energy resolution of 0.3-0.4 eV. The Me $L_{2,3}$ XES were measured with an energy resolution of 0.7-0.8 eV.

The XPS measurements were performed with an ESCA spectrometer of Physical Electronics (PHI 5600 ci) with monochromatized Al K_α radiation of a 0.3 eV FWHM. The energy resolution of the analyzer was 1.5% of the pass energy. The pressure in the vacuum chamber during the measurements was below 5×10^{-9} mbar. Prior to XPS measurements, the samples were fractured in ultra-high vacuum. All photoemission studies were performed at room temperature on freshly cleaved surfaces. Charging of the insulating $\text{Me}[\text{N}(\text{CN})_2]_2$ samples was compensated with an electron gun. Because there is no saturated carbon in these molecules, the binding energies can not be corrected using the C $1s$ line. Therefore we have used an alternative way¹¹ of fixing the N $1s$ line of the cyanide group at 399.6 eV.

Polycrystalline pressed pellets of $\text{Me}[\text{N}(\text{CN})_2]_2$ compounds were used for XES and XPS measurements. Details about the sample preparation can be found in Refs. 6 and 7.

Diffuse reflectance spectroscopy on powder samples was used to measure the lowest electronic transition observable in the visible region, which can be interpreted as possible band gap energies. The reflectance spectra were taken on powdered samples at room temperature in a 1-mm quartz cuvette which was illuminated by light from a 75-watt Xe high-pressure arc lamp. The reflected light was admitted into an Acton Spectropro 300i 300 mm spectrometer with a Hamamatsu CCD detector, which gave light intensities versus wavelength from 300 to 800 nm. The spectrum of a "white" standard, consisting of powdered NaCl, was used for determination of the absorbance, $\log(I_0/I_s)$, as a function of wavelength for each sample, where I_0 is the intensity of the "white" standard and I_s is the intensity of the sample compound.

For comparison with the experimental results, electronic-structure calculations were performed for ferromagnetic (FM), antiferromagnetic (AF), and nonmagnetic (NM) phases using the crystal structures determined from x-ray and neutron diffraction experiments.^{3,5,6,7,8} Spins were restricted to be collinear. Calculations were carried out using the VASP program,¹² a density-functional-based code employing planewave basis sets and ultrasoft pseudopotentials. The electron-electron interaction was treated in the generalized gradient approximation (GGA),^{13,14} and electronic wave functions were expanded in planewaves up to a kinetic energy cutoff of 435 eV. Monkhorst-Pack meshes¹⁵ of up to $8 \times 8 \times 8$ \mathbf{k} -points were used to sample the Brillouin zone, and the linear tetrahedron method was used to integrate over the Brillouin zone.

III. MAGNETIC PROPERTIES

Table I summarizes the results of the total-energy calculations. Density-functional-theory (DFT) calculations for terminated cluster models yield similar results.¹⁶ Experimentally, $\text{Mn}[\text{N}(\text{CN})_2]_2$ and $\text{Fe}[\text{N}(\text{CN})_2]_2$ are both canted antiferromagnets. In the Mn compound, the canting angle is reported to be at most a few degrees,⁶ while in the Fe compound, the canting angle is estimated to be 20-23°.⁸ Our calculations find $\text{Mn}[\text{N}(\text{CN})_2]_2$ to be antiferromagnetic, but neglect of both the canting and spin-orbit interaction in $\text{Fe}[\text{N}(\text{CN})_2]_2$ results in the FM phase being favored. Similar results were recently obtained in Ref. 17. We expect that when spins are not restricted to be collinear, density functional theory would yield an AF ground state for $\text{Fe}[\text{N}(\text{CN})_2]_2$. For $\text{Ni}[\text{N}(\text{CN})_2]_2$ and $\text{Co}[\text{N}(\text{CN})_2]_2$, we find the ground state to be ferromagnetic, in agreement with experiments. In the case of $\text{Cu}[\text{N}(\text{CN})_2]_2$, the FM and AF phases are calculated to be very close in energy and favored over the NM phase. Magnetization studies show no long-range ordering above 2 K,⁵ but a recent study⁸ finds that $\text{Cu}[\text{N}(\text{CN})_2]_2$ becomes ferromagnetic at lower temperatures with $T_c \sim 1.8$ K. Hence we report results of our calculations for the FM phase.

In superexchange systems, the magnitude and sign of the one-electron contribution to the exchange interaction depend on the filling of those orbitals on neighboring magnetic centers that interact via a bridging ligand.^{18,19,20} The relevant orbitals, *i.e.*, those with non-zero interaction matrix elements, depend in turn on the geometry of the superexchange pathway. The magnetic ordering is thus determined by an interplay between the occupation of the d shell and the superexchange angle. In $\text{Me}[\text{N}(\text{CN})_2]_2$, neighboring Me sites are connected through a Me-[N-C-N]-Me pathway, where the two N sites along the path are inequivalent. The Me-[N-C-N]-Me angle increases monotonically in going from $\text{Mn}[\text{N}(\text{CN})_2]_2$ to $\text{Ni}[\text{N}(\text{CN})_2]_2$, with a total change of about 2.5 degrees.⁶ It has been suggested that this structural change in the pathway is responsible for the different magnetic ground states in the dicyanamides, with the angle passing through a critical value in going across the $3d$ series.⁶ Our calculations find that such small changes in structure do not change the energetic ordering of the magnetic phases. The occupation of the $3d$ shell is evidently a more significant factor in determining the sign of the superexchange interaction in these systems.

Density functional theory typically underestimates magnetic moments, but, as shown in Table I, discrepancies for Me = Fe and Ni appear unusually large. This is likely because the measured magnetic moments in the table, determined from neutron powder diffraction studies,^{6,8} include both spin and orbital contributions. For octahedrally coordinated Me^{2+} cations without spin-orbit coupling, the orbital moment is expected to be completely quenched for Me = Mn, Ni, and Cu, and unquenched or partially quenched for Me = Fe and Co.²¹ With spin-orbit coupling, the quenching due to the crystal field is incomplete, resulting in a Landé g -factor that can deviate from 2.^{7,8} With no mechanism for unquenching the orbital moment within our calculations, a direct comparison between the theoretical and experimental moments in Table I is not appropriate.

It is well known that the local spin magnetic moment is related to spectral splitting of the $3s$ core-level x-ray photoemission spectra in transition metals and their compounds. The splitting originates from the exchange coupling between the $3s$ hole and the $3d$ electrons and the magnitude of the splitting is proportional to $(2S+1)$, where S is the local spin of the $3d$ electrons in the ground state.²² The $3s$ spectra of the $\text{Me}[\text{N}(\text{CN})_2]_2$ materials together with those of simple oxides MnO, FeO, CoO, NiO, and CuO are shown in Fig. 1. Peaks A and B denote $3s^{-1}3d^{n+1}L^{-1}$ final-state configurations, and C and D denote $3s^{-1}3d^n$ final-state configurations, where L^{-1} denotes a ligand hole due to the charge-transfer process. For $\text{Mn}[\text{N}(\text{CN})_2]_2$, fitting curves and their component peaks are shown. The Mn $3s$ spectrum shows two peaks, C and D, which can be attributed to the $3s^{-1}3d^5$ final state. The magnitude of the $3s$ exchange splitting in $\text{Mn}[\text{N}(\text{CN})_2]_2$, 6.5 eV, is very similar to that in MnO, 6.2 eV,²³ which indicates the Mn $3d^5$ ground-state configuration for $\text{Mn}[\text{N}(\text{CN})_2]_2$. This correlates well with calculated and measured spin moments of $\text{Mn}[\text{N}(\text{CN})_2]_2$ presented in Table I. The Me $3s$ spectra of $\text{Ni}[\text{N}(\text{CN})_2]_2$, $\text{Co}[\text{N}(\text{CN})_2]_2$, and $\text{Fe}[\text{N}(\text{CN})_2]_2$ show a complex structure formed by both $3s^{-1}3d^n$ and $3s^{-1}3d^{n+1}L^{-1}$ final-state configurations. Coexistence of both exchange and charge-transfer effects makes the comparison of the Me $3s$ splitting with the local magnetic moments difficult. Similarities with the spectra of the monoxides suggest that the Me $3s$ energy splitting is systematically reduced with increasing Me atomic number, as expected for transition metal ions with nominal 2^+ valence (Table I). For $\text{Cu}[\text{N}(\text{CN})_2]_2$, the exchange splitting is expected for the $3s^{-1}3d^9$ configuration only, which is localized in the energy interval from 130 to 135 eV. Low energy resolution limits our ability to separate this splitting in the present data, but it has been observed in copper oxides (see Fig. 1 and Ref. 24).

IV. ELECTRONIC STRUCTURE

Figure 2 shows the measured carbon and nitrogen K_α XES of the $\text{Me}[\text{N}(\text{CN})_2]_2$ compounds. As seen, the carbon K_α XES (Fig. 2a) are very similar across the series because of the same local atomic and electronic structure of carbon atoms in cyano groups. On the other hand, the nitrogen atoms occupy two non-equivalent sites in the crystal structure of $\text{Me}[\text{N}(\text{CN})_2]_2$ compounds, where each Me atom has two N(1) neighbors along the long axis and four N(2) neighbors

from CN anions along the other axes.⁶ The nitrogen K_α XES of $\text{Me}[\text{N}(\text{CN})_2]_2$ (Fig. 2b) has contributions from both sites. The N K_α spectrum of the reference compound $\text{Na}_4\text{Fe}(\text{CN})_6(\text{OH}_2\text{O})$ (Fig. 2b) shows N contributions from cyano groups and is quite different from the non-resonant nitrogen spectra of $\text{Me}[\text{N}(\text{CN})_2]_2$. In our XPS measurements, the N $1s$ spectrum is split into two main lines separated by approximately 1.6 eV, corresponding to the difference in the N $1s$ binding energies of the two non-equivalent N sites (Table II).

Additional measurements were made for resonantly excited nitrogen K_α XES in $\text{Mn}[\text{N}(\text{CN})_2]_2$. The energy dependence of the spectra when the excitation energy was tuned near the N $1s$ threshold is shown in Fig. 3a. The intensities of the peaks at 389.9, 392.7 and 394.8 eV change with excitation energy. The non-resonant spectrum d excited far from the N $1s$ threshold can be described as a superposition of spectra b and c (Fig. 3b), corresponding to contributions from selectively excited non-equivalent nitrogen atoms. Based on our measurements of the non-resonant N K_α XES of $\text{Na}_4\text{Fe}(\text{CN})_6(\text{OH}_2\text{O})$ (Fig. 2b), we can attribute the origin of the resonant spectrum of $\text{Mn}[\text{N}(\text{CN})_2]_2$ excited near peaks a and b of the N $1s$ TEY to N(2) atoms located in cyano groups, whereas the spectrum excited near peak c of the N $1s$ TEY can be explained by contributions from both N(1) and N(2) atoms.

The valence band (VB) XPS and the XES of the constituents of $\text{Me}[\text{N}(\text{CN})_2]_2$ are compared in Figs. 4-8. We have selected for this comparison the non-resonant carbon and nitrogen K_α XES shown in Fig. 2 and the Me L_3 XES ($3d_{4s} \rightarrow 2p_{3/2}$ transition) which were excited just above the L_3 threshold to exclude the excitation of the Me L_2 XES ($3d_{4s} \rightarrow 2p_{1/2}$ transition) that overlaps the Me L_3 XES due to spin-orbit splitting. To convert the XES of the constituents to the binding-energy scale, we have subtracted emission energies from the XPS binding energies of core levels (Table II). According to this comparison, the top of the valence band (a) is derived mainly from Me $3d$ and N $2p$ states. Towards the middle of the valence band the Me $3d$, N $2p$ and C $2p$ states are strongly hybridized, forming a broad structure (b-d). At the bottom of the valence band (e) are mixed carbon and nitrogen $2p$ states. Atomic-like carbon and nitrogen $2s$ states are located in region (f), with binding energy around 20-25 eV.

For comparison, we present theoretical results for $\text{Ni}[\text{N}(\text{CN})_2]_2$ as an example. The calculated electronic density of states (DOS) of $\text{Ni}[\text{N}(\text{CN})_2]_2$ is shown in Fig. 9. The total DOS is in the lowest panel, and site- and l -projected DOS are plotted in the other panels. In the lowest panel, a Gaussian broadening of 1.0 eV has been introduced to simulate the effect of finite instrumental resolution. The partial DOS in the upper three panels have been broadened by 0.2 eV to help in identifying features seen in the experimental XES spectra. Features in the DOS are labeled (a)-(f) as in the experimental XPS spectra. The nature of the states at different energies is generally consistent with what is found in the XPS/XES comparison. Regions (a) and (b) near the top of the valence band are dominated by Ni $3d$ states, with some hybridization with C and N $2p$ states, and they correspond to the peak in the Ni L_3 XES spectrum. Regions (c) and (d) contain strong contributions from C $2p$ and N $2p$ states, as seen in the C and N XES spectra, as well as some Ni $3d$ states. Peak (e), approximately 12 eV below the top of the valence band, is primarily of C $2p$ and C $2s$ character, and N $2p$ contributions from N(1) sites. Region (f) has significant contributions from the N $2s$, C $2s$, and C $2p$ states and is observed in the C K_α XES spectrum.

For the other compounds, the electronic DOS is very similar to that of $\text{Ni}[\text{N}(\text{CN})_2]_2$ from about 25 eV below the top of the valence band up to region (d) where $3d$ states of the transition metal start playing a significant role. The hybridization between N $2p$ and Me $3d$ states increases with the Me atomic number. For Me = Mn, Fe, and Co, states near the top of the valence band are overwhelmingly of Me d character, while for Me = Ni and Cu, the relative contribution of N p states is increased. In both the calculations and the experiments, the weight of the $3d$ -derived bands shifts with respect to the top of the valence band. Based on the XPS valence bands, the maximum of the $3d$ bands varies from about 4 eV for $\text{Mn}[\text{N}(\text{CN})_2]_2$ to about 6 eV for $\text{Cu}[\text{N}(\text{CN})_2]_2$ (see Figs. 4-8 and Table II). This result is confirmed by the Me L_3 XES converted to the binding-energy scale. In addition, in the calculations, we find, for example, about a 1.5 eV difference in the position of the main maxima of the occupied d -DOS weights in $\text{Cu}[\text{N}(\text{CN})_2]_2$ compared to $\text{Ni}[\text{N}(\text{CN})_2]_2$ (Fig. 10), which is similar to what is observed experimentally (Table II). The deepening of $3d$ states found for $\text{Cu}[\text{N}(\text{CN})_2]_2$ is due to the localization d electrons at the end of the $3d$ series. This is observed in molecular crystals because the $d-d$ and $d-sp$ interactions are weaker than in conventional divalent (and even monovalent) copper compounds. The decreasing exchange splitting is likely an additional factor affecting energy deepening of $3d$ states.

The deepening of d states across the series is accompanied by a shift towards higher binding energies of the maxima of the Me $2p$ and Me $3s$ XPS spectra of $\text{Me}[\text{N}(\text{CN})_2]_2$ in comparison with those for $3d$ monoxides.^{23,24} This shift increases from about 0 eV for $\text{Mn}[\text{N}(\text{CN})_2]_2$ to about 3 eV for $\text{Cu}[\text{N}(\text{CN})_2]_2$. Due to weak metal-metal interactions in molecular crystals, especially in $\text{Cu}[\text{N}(\text{CN})_2]_2$ where $3d$ states are strongly localized, the screening of the final states is weaker than in the other cases, resulting in larger binding energies of the valence bands and the core levels.

At the top of the valence band the detailed electronic structure is determined by the filling of the transition metal $3d$ states. The local environment around Me sites is a distorted octahedron of N sites, and the ligand field splits the $3d$ states by approximately 1.5 eV into t_{2g} and e_g manifolds. In $\text{Mn}[\text{N}(\text{CN})_2]_2$, with an exchange splitting of over 3 eV, the majority d bands are fully occupied and there is a significant gap to the unoccupied minority d bands.⁹ As the number of d electrons increases, the ligand-field splitting stays about the same while the exchange splitting decreases.

The majority bands nevertheless remain full. The minority t_{2g} bands are narrow and split by the tetragonal distortion of the local octahedral environment and by the longer-range crystal field. In the FM configuration, intersublattice $d-d$ interactions broaden the majority t_{2g} bands, resulting in a two-fold subband of $d_{xz,yz}$ states with a gap to the d_{xy} subband. (Axes are referenced to the local octahedral environment.) In the AF configuration, intersublattice $d-d$ interactions are suppressed, which narrows the t_{2g} bands. For Me = Fe, the ordering of the one-fold and two-fold subbands reverses in the FM phase. Thus, with one minority t_{2g} electron per Fe site, AF Fe[N(CN)₂]₂ is metallic while FM Fe[N(CN)₂]₂ is insulating, as shown in Fig. 11. The lack of a gap in AF Fe[N(CN)₂]₂ with collinear spins contributes to its instability with respect to the insulating FM phase. In FM Co[N(CN)₂]₂, the two-fold subband fills, and in FM Ni[N(CN)₂]₂, the t_{2g} manifold is completely occupied. The Jahn-Teller effect significantly enhances the tetragonal distortion of the octahedral environment around Cu sites in Cu[N(CN)₂]₂,^{4,5} which increases the splitting between e_g bands. The calculated GGA band gaps are listed in Table I, along with estimated gaps from diffuse reflectance spectroscopy. The agreement is better for the compounds where t_{2g} band is either completely empty or completely full.

The narrow width of some of the d bands (Fig. 11) suggests that electron correlations could be important in these materials. Additional evidence for this is the GGA's large underestimation of the band gaps in some of the compounds, particularly Co[N(CN)₂]₂. Furthermore, the fact that the measured magnetic moments in Fe[N(CN)₂]₂ and Ni[N(CN)₂]₂ are larger than the maximum moments that could be created by spin alone indicates the importance of the orbital moment, and therefore methods incorporating orbital dependence of the potential could significantly improve the results. The situation is reminiscent of the monoxides of the $3d$ transition metals. As with the oxides, it is likely that methods beyond DFT-GGA are needed for a better description of the electronic and magnetic structure of the dicyanamides in the solid state.

V. CONCLUSIONS

We have carried out a theoretical and experimental investigation of the electronic structure of the Me[N(CN)₂]₂ (Me = Mn, Fe, Co, Ni, Cu) molecular magnets. The general features of the valence bands are similar across the series, with the primary exceptions being the location of the $3d$ bands with respect to the Fermi level and the degree of hybridization between Me $3d$ states and N $2p$ states. Going across the row from Mn to Cu, the d bands lie deeper in energy, and the degree of hybridization with N p states increases.

Total-energy calculations indicate that the small differences in structural parameters (for example, the angle of the superexchange pathway) found in these isostructural materials is not sufficient to account for differences in their magnetic ground states. Rather, the occupation of the $3d$ shell is likely a more significant factor.

For most of the materials in the series, our calculations underestimate either the band gap or the local magnetic moment. Together with the existence of narrow d -bands in these materials, this suggests that a better description of the magnetic and electronic structure of these materials will require a more accurate treatment of electron-electron interactions.

Acknowledgments

The authors thank M. R. Pederson for helpful discussions and for communicating unpublished results. This work was supported by the Research Council of the President of the Russian Federation under Grant NSH-1026.2003.2, the Russian Foundation for Basic Research under Project 02-02-16674, the President's NSERC fund of the University of Saskatchewan, Deutsche Forschungsgemeinschaft (DFG) under the priority programme SPP 1137 Molekularer Magnetismus, the US National Science Foundation under Grant DMR-0210717, and the US Office of Naval Research under Grant N00014-02-1-1046. Work at the Advanced Light Source at Lawrence Berkeley National Laboratory was supported by the U.S. Department of Energy under Contract No. DE-AC03-76SF00098. Work at the Advanced Photon Source is supported by the U.S. Department of Energy, Office of Science, Office of Basic Energy Sciences under Contract No. W-31-109-ENG-38.

¹ J. M. Manriquez, G. T. Yee, R. S. McLean, A. J. Epstein, and J. S. Miller, *Science* **252**, 1415 (1991).

² S. Ferlay, T. Mallah, R. Ouahes, P. Veillet, and M. Verdagner, *Nature* **378**, 701 (1995).

³ J. L. Manson, C. R. Kmetz, Q. Huang, J. W. Lynn, G. M. Bendele, S. Pagola, P. W. Stephens, L. M. Liable-Sands, A. L. Rheingold, A. J. Epstein, and J. S. Miller, *Chem. Mater.* **10**, 2552 (1998).

- ⁴ S. R. Batten, P. Jensen, B. Moubaraki, K. S. Murray, and R. Robson, *Chem. Commun.* **3**, 439 (1998).
- ⁵ M. Kurmoo and C. J. Kepert, *New J. Chem.* **22**, 1515 (1998).
- ⁶ C. R. Kmety, Q. Huang, J. W. Lynn, R. W. Erwin, J. L. Manson, S. McCall, J. E. Crow, K. L. Stevenson, J. S. Miller, and A. J. Epstein, *Phys. Rev. B* **62**, 5576 (2000).
- ⁷ C. R. Kmety, J. L. Manson, Q. Huang, J. W. Lynn, R. W. Erwin, J. S. Miller, A. J. Epstein, *Phys. Rev. B* **60**, 60 (1999).
- ⁸ C. R. Kmety, Ph.D. Thesis, The Ohio State University, 2000.
- ⁹ M. R. Pederson, A. Y. Liu, T. Baruah, E. Z. Kurmaev, A. Moewes, S. Chiuzbäian, M. Neumann, C. R. Kmety, K. L. Stevenson, D. Ederer, *Phys. Rev. B* **66**, 014446 (2002).
- ¹⁰ J. J. Jia, T. A. Callcott, J. Yurkas, A. W. Ellis, F. J. Himpsel, M. G. Samant, J. Stöhr, D. L. Ederer, J. A. Carlisle, E. A. Hudson, L. J. Terminello, D. K. Shuh, and R. C. C. Perera, *Rev. Sci. Instrum.* **66**, 1394 (1995).
- ¹¹ G. Beamson, D. Briggs, *High Resolution XPS of Organic Polymers: the Scienta ESCA300 Database* (Wiley, Chichester, 1992).
- ¹² G. Kresse and J. Furthmüller, *Comput. Mater. Sci.* **6**, 15 (1996); *Phys. Rev. B* **54**, 11169 (1996).
- ¹³ Y. Wang and J. P. Perdew, *Phys. Rev. B* **44**, 13298 (1991).
- ¹⁴ J. P. Perdew, K. Burke, and M. Ernzerhof, *Phys. Rev. Lett.* **77**, 3865 (1996).
- ¹⁵ H. J. Monkhorst and J. D. Pack, *Phys. Rev. B* **13**, 5188 (1976).
- ¹⁶ M. R. Pederson and T. Baruah (private communication).
- ¹⁷ E. Ruiz, *J. Solid State Chem.* (to be published).
- ¹⁸ P. W. Anderson, *Phys. Rev.* **79**, 350 (1950); *Phys. Rev.* **115**, 2 (1959).
- ¹⁹ J. B. Goodenough, *Magnetism and the Chemical Bond* (Wiley, New York, 1963).
- ²⁰ H. Weihe, H. U. Güdel, H. Toftlund, *Inorg. Chem.* **39**, 1351 (2000).
- ²¹ B. N. Figgis, *Introduction to Ligand Fields* (Wiley, New York, 1966).
- ²² J. H. Van Vleck, *Phys. Rev. B* **45**, 405 (1934).
- ²³ V. R. Galakhov, M. Demeter, S. Bartkowski, M. Neumann, N. A. Ovechkina, E. Z. Kurmaev, N. I. Lobachevskaya, Ya. M. Mukowskii, J. Mitchell, D. L. Ederer, *Phys. Rev. B* **65**, 113102 (2002).
- ²⁴ V. R. Galakhov, L. D. Finkelstein, D. A. Zatsepin, E. Z. Kurmaev, A. A. Samokhvalov, S. V. Naumov, G. K. Tatarinova, M. Demeter, S. Bartkowski, M. Neumann, and A. Moewes, *Phys. Rev. B* **62**, 4922 (2000).
- ²⁵ C. R. Kmety, J. L. Manson, S. McCall, J. E. Crow, K. L. Stevenson, and A. J. Epstein, *J. Magn. Magn. Mater.* **248**, 52 (2002).

FIG. 1: Me $3s$ x-ray photoelectron spectra of $\text{Me}[\text{N}(\text{CN})_2]_2$ (points) and simple oxides MeO (thick lines). The maxima of the Me $3s$ spectra of monoxides have been shifted in binding energy to facilitate comparison with the $\text{Me}[\text{N}(\text{CN})_2]_2$ spectra. For $\text{Me}[\text{N}(\text{CN})_2]_2$, fitting curves are shown with thin lines.

FIG. 2: Non-resonant (a) carbon and (b) nitrogen K_α XES of $\text{Me}[\text{N}(\text{CN})_2]_2$ compounds. The N K_α XES for the reference compound $\text{Na}_4\text{Fe}(\text{CN})_6(\text{OH}_2\text{O})$ is included for comparison.

FIG. 3: Resonant N K_α XES of $\text{Mn}[\text{N}(\text{CN})_2]_2$. Spectra obtained with different excitation energies near the N $1s$ threshold are shown in (a). The non-resonant spectrum d is compared to superpositions of resonant spectra a , b , and c in (b). The non-resonant spectrum is better represented by a superposition of b and c than by a superposition of a and c .

FIG. 4: Comparison of XPS VB and XES of constituents for $\text{Mn}[\text{N}(\text{CN})_2]_2$ in the binding energy scale.

FIG. 5: Comparison of XPS VB and XES of constituents for $\text{Fe}[\text{N}(\text{CN})_2]_2$ in the binding energy scale.

FIG. 6: Comparison of XPS VB and XES of constituents for $\text{Co}[\text{N}(\text{CN})_2]_2$ in the binding energy scale.

FIG. 7: Comparison of XPS VB and XES of constituents for $\text{Ni}[\text{N}(\text{CN})_2]_2$ in the binding energy scale.

FIG. 8: Comparison of XPS VB and XES of constituents for $\text{Cu}[\text{N}(\text{CN})_2]_2$ in the binding energy scale.

FIG. 9: Total and partial density of states calculated for ferromagnetic $\text{Ni}[\text{N}(\text{CN})_2]_2$. The total DOS in the bottom panel has been broadened by 1.0 eV, while the site-projected DOS in the top three panels have been broadened by 0.2 eV.

FIG. 10: Cu and Ni d -densities of states calculated for FM $\text{Cu}[\text{N}(\text{CN})_2]_2$ and FM $\text{Ni}[\text{N}(\text{CN})_2]_2$. To emphasize gross features in the DOS, Methfessel-Paxton (fifth order) smearing of 1 eV is used. The band gaps are masked by this broadening, and the Fermi level is set to 0 eV. The inset shows total FM $\text{Cu}[\text{N}(\text{CN})_2]_2$ densities of states calculated with the linear tetrahedron method.

FIG. 11: Fe d -density of states calculated for $\text{Fe}[\text{N}(\text{CN})_2]_2$ with (a) AF spin ordering and (b) FM spin ordering. The linear tetrahedron method is used to calculate the DOS.

TABLE I: Calculated total-energy differences between different spin configurations (in eV/Me site), local spin magnetic moments (in μ_B), and band gaps (in eV). For Me = Mn and Fe, the calculated spin moments and gaps are given for the antiferromagnetic state, while for Me = Co, Ni, and Cu, results for the ferromagnetic state are presented. Experimental moments from neutron powder diffraction experiments reported in Refs. 6,7,25 are shown for comparison and include both spin and orbital contributions. Estimates for band gaps obtained from diffuse reflectance spectroscopy on powder samples at room temperature are also included.

	ΔE		μ_{Me}		E_g	
	NM-AF	AF-FM	calc	expt	calc	expt
Mn[N(CN) ₂] ₂	2.490	-0.018	4.50	4.61	2.12	2.07
Fe[N(CN) ₂] ₂	0.862	0.025	3.59	4.53	0.00 ^a	1.46
Co[N(CN) ₂] ₂	0.735	0.023	2.54	2.67	0.24	2.40
Ni[N(CN) ₂] ₂	0.939	0.015	1.59	2.21	1.36	1.97
Cu[N(CN) ₂] ₂	0.287	0.000	0.65	1.05	0.52	1.91

^aCalculations yield metallic state for AF Fe[N(CN)₂]₂ (see text).

TABLE II: XPS core level binding energies and location of 3*d*-band maxima (in eV) of Me[N(CN)₂]₂, with Me = Mn, Fe, Co, Ni, Cu.

	Mn[N(CN) ₂] ₂	Fe[N(CN) ₂] ₂	Co[N(CN) ₂] ₂	Ni[N(CN) ₂] ₂	Cu[N(CN) ₂] ₂
C 1 <i>s</i>	287.7	287.7	287.1	288.0	288.0
N 1 <i>s</i>	399.6; 398.0	399.6; 398.3	399.6; 398.5	399.6; 397.2	399.6; 397.8
Me 2 <i>p</i> _{3/2}	642.4	710.1	782.2	857.2	936.5
Me 3 <i>d</i>	4.0	4.1	4.2	4.7	6.0

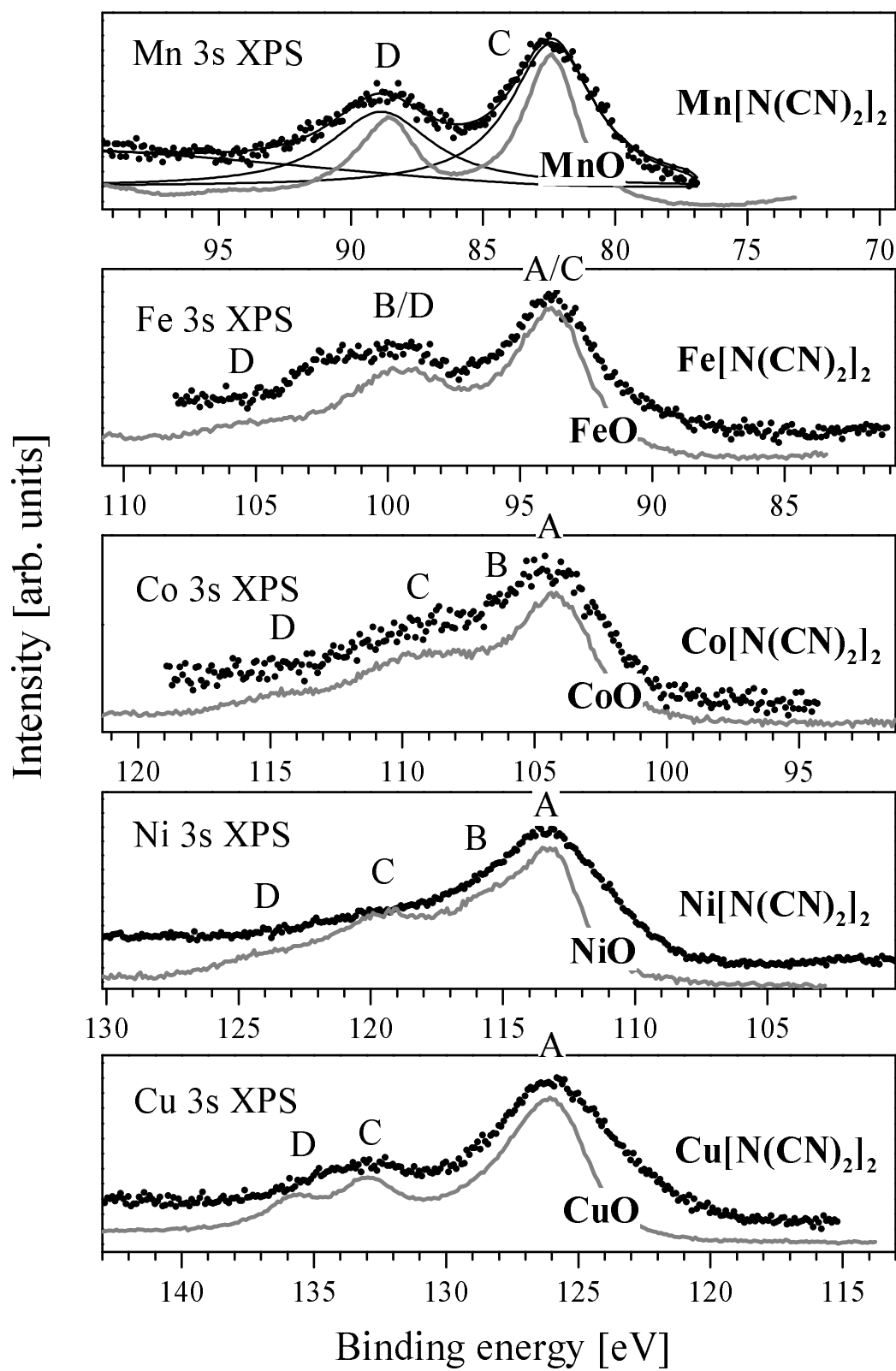


Fig. 1

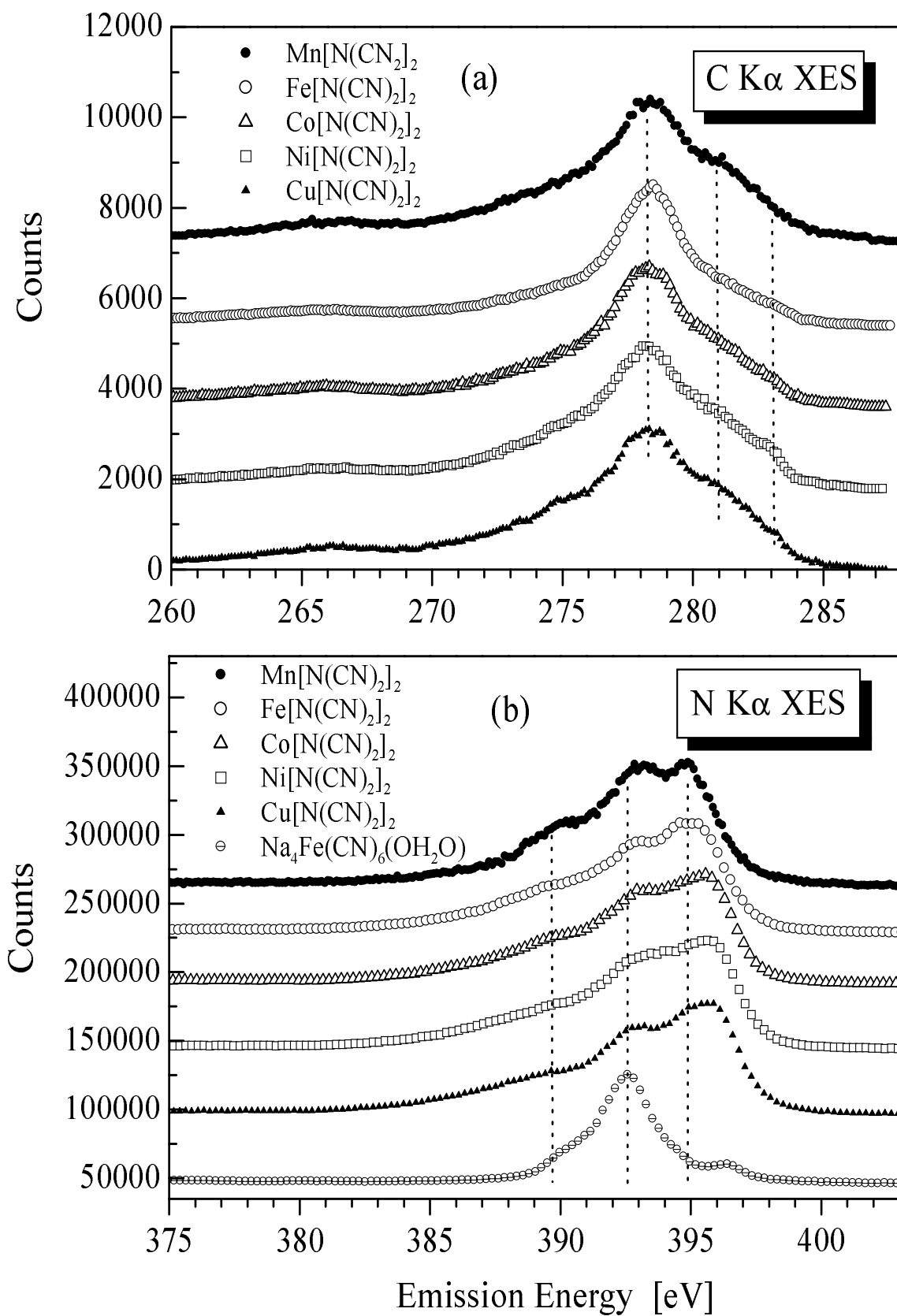


Fig. 2

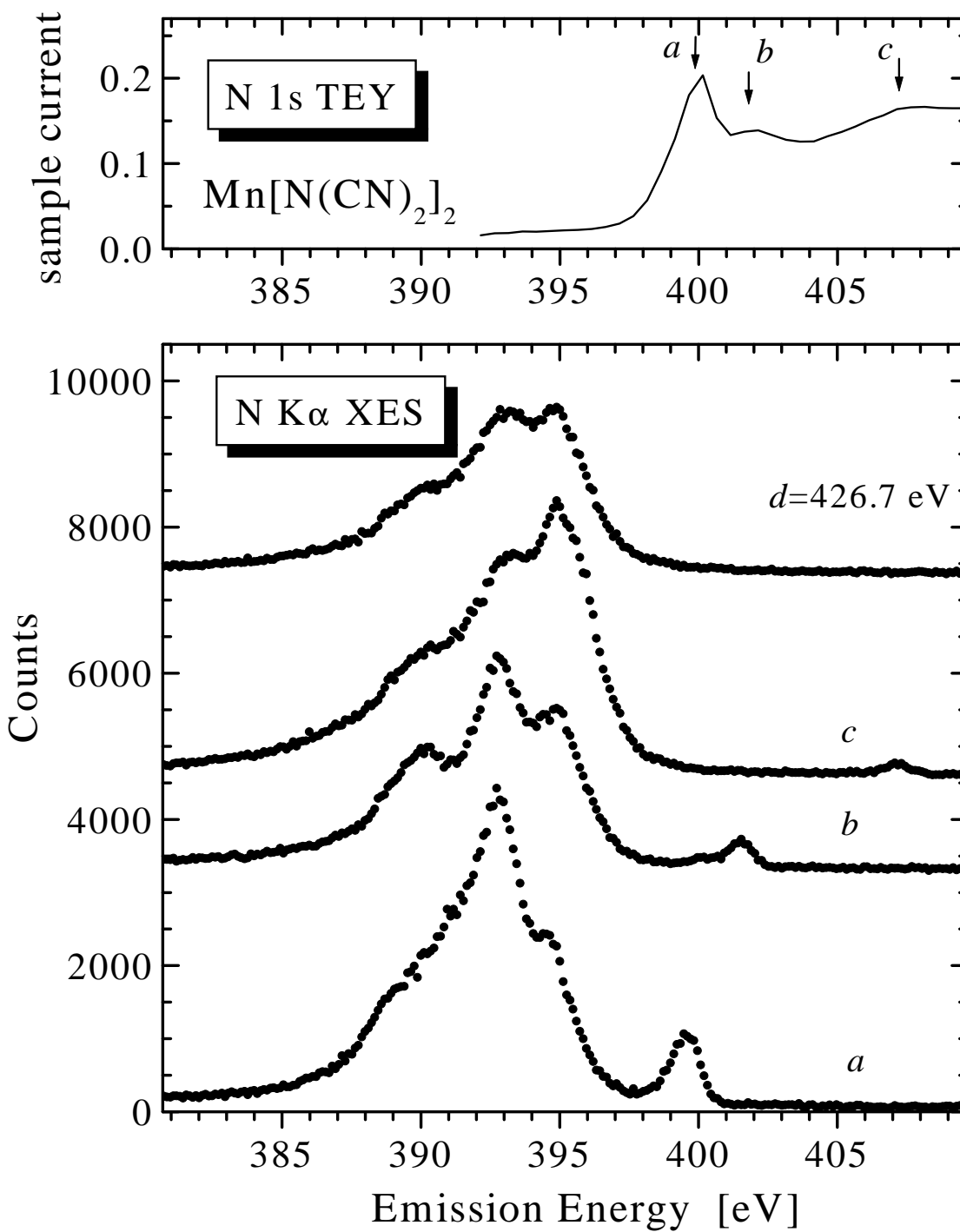


Fig. 3a

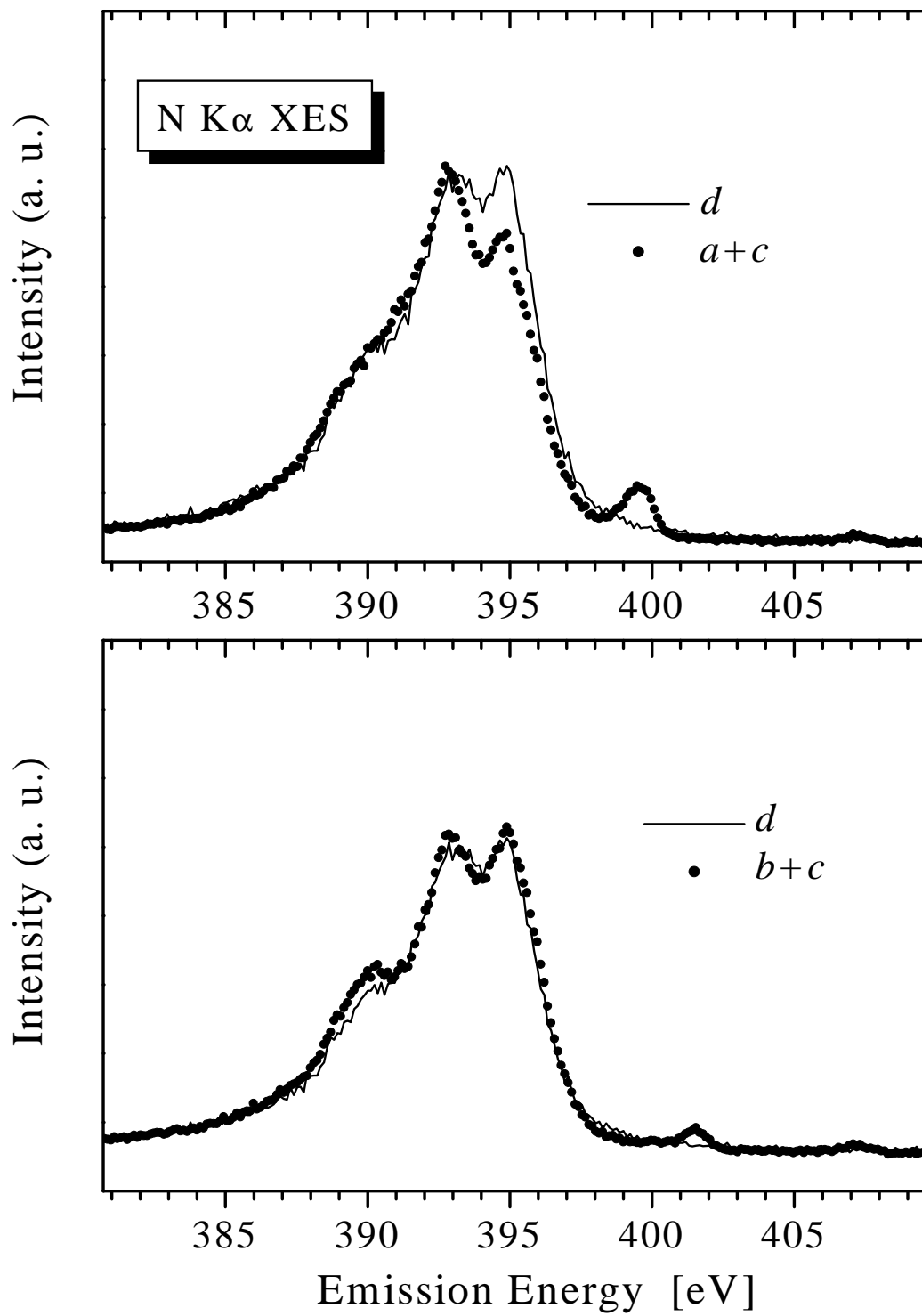


Fig. 3b

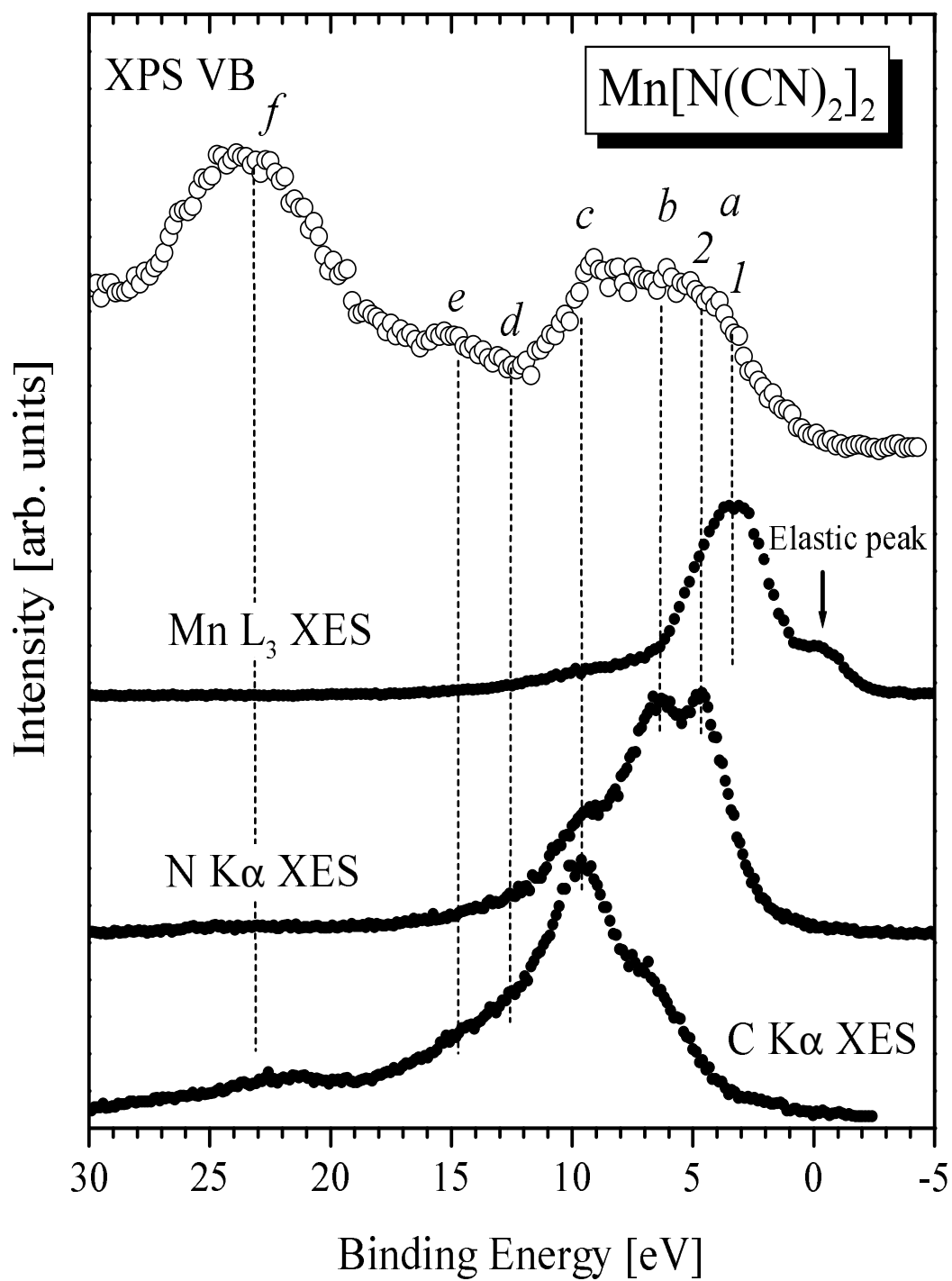


Fig. 4

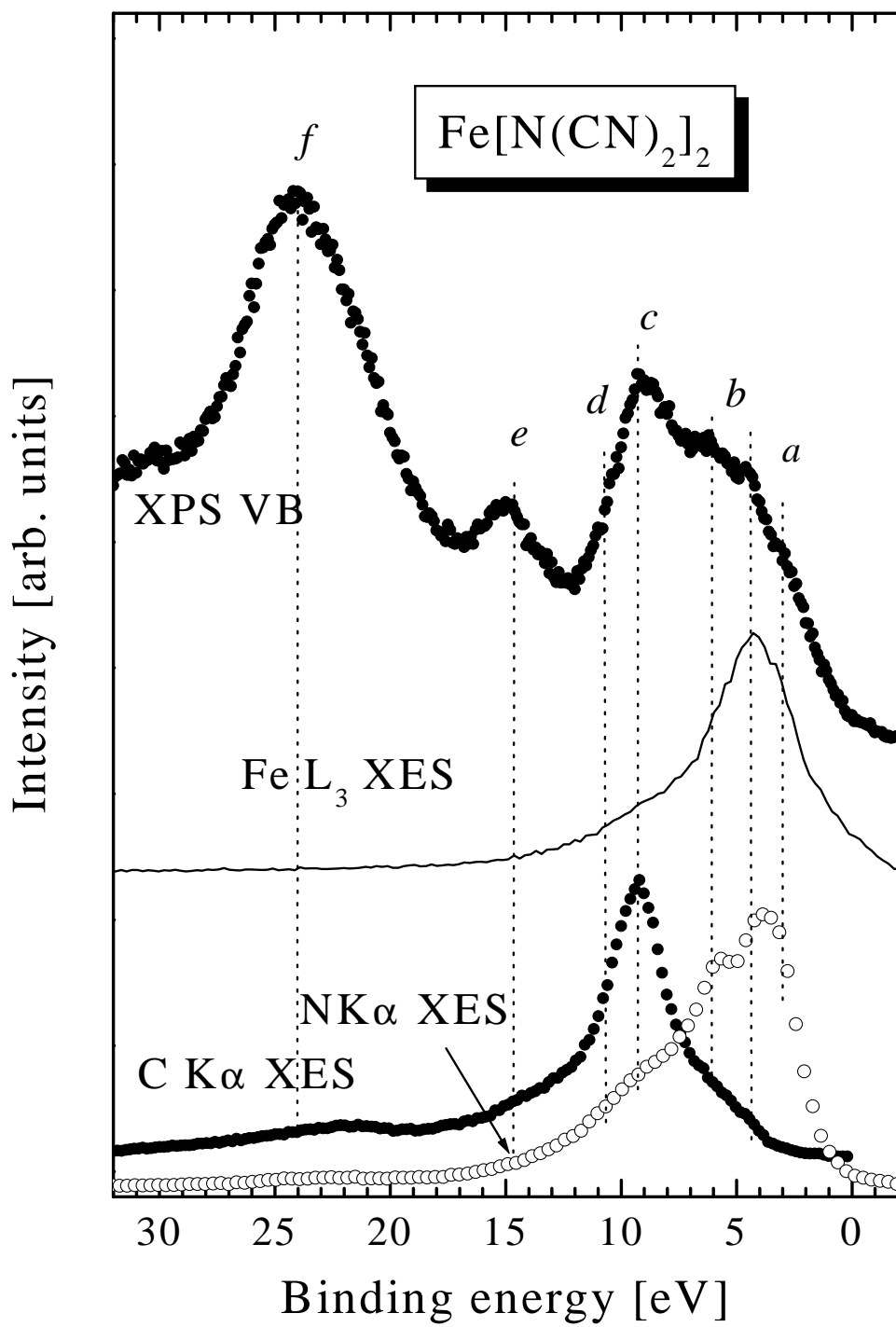


Fig. 5

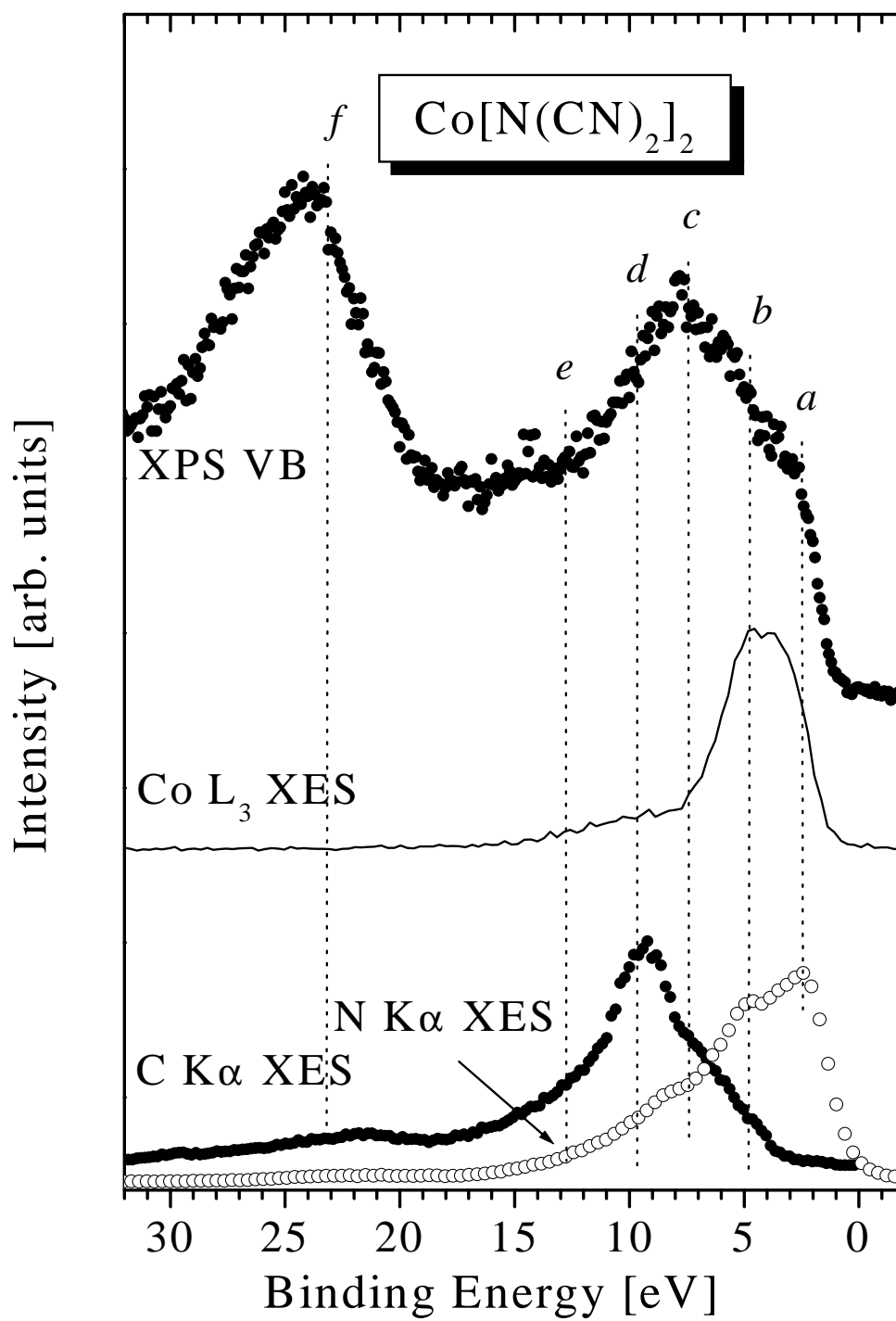


Fig. 6

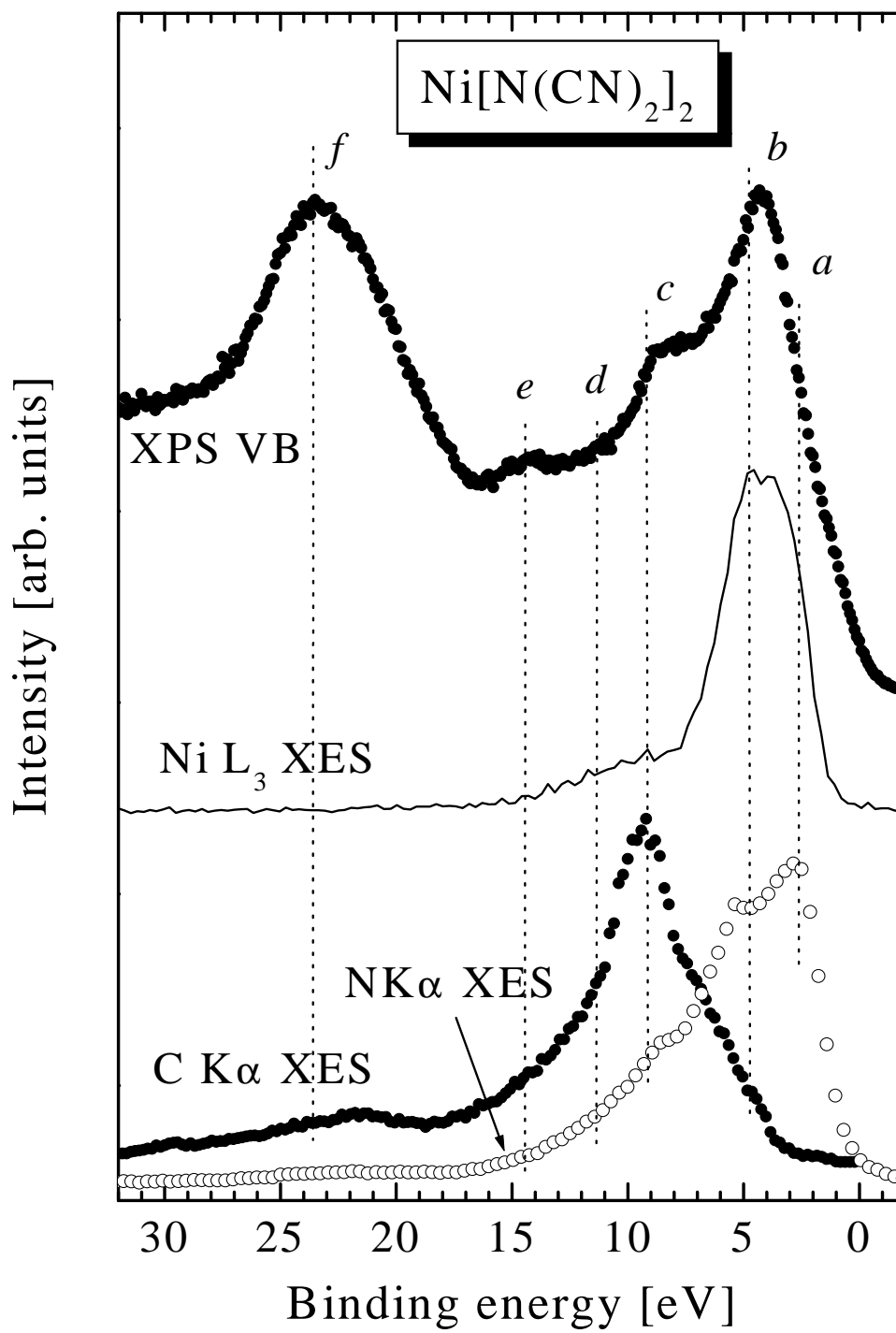


Fig. 7

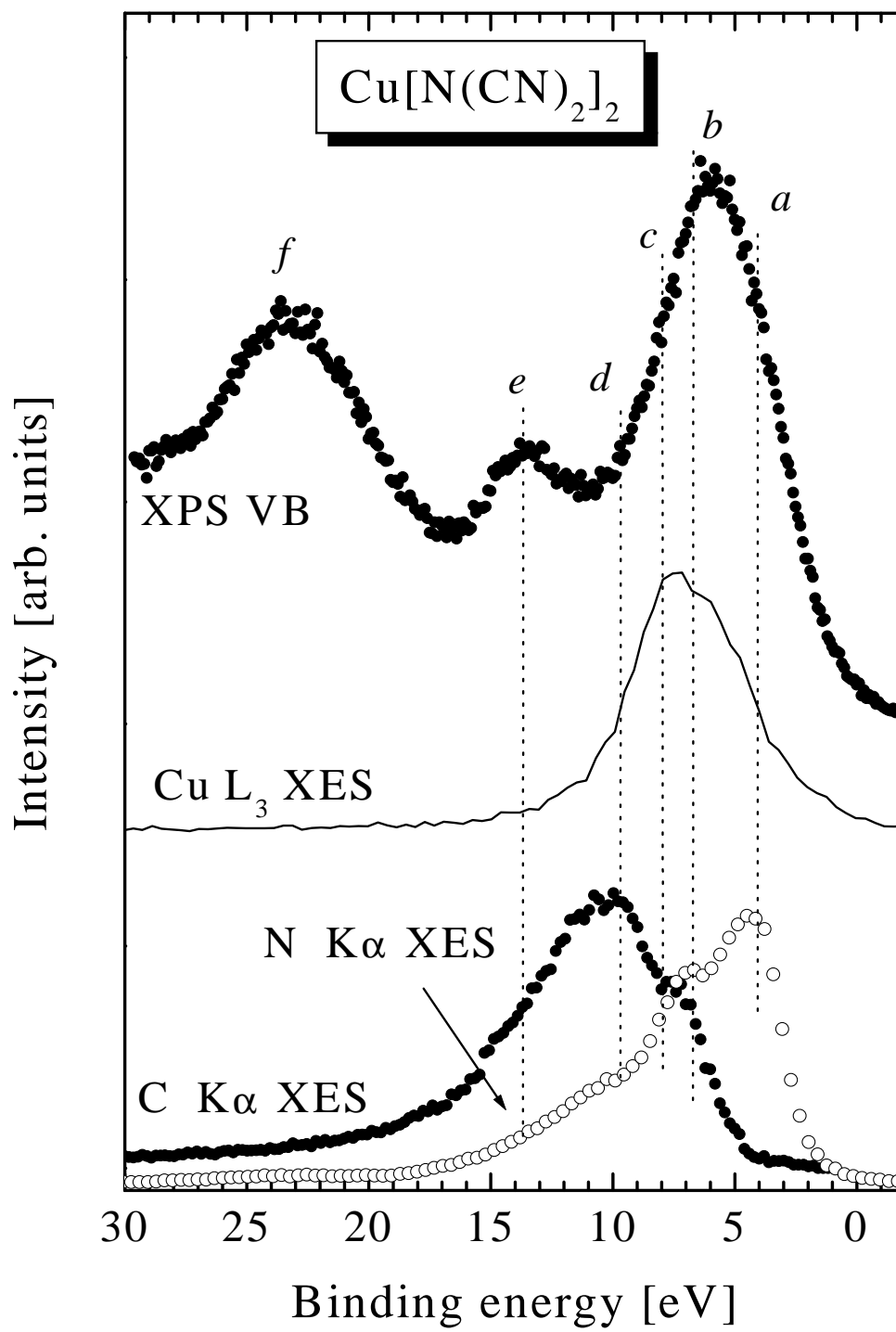


Fig. 8

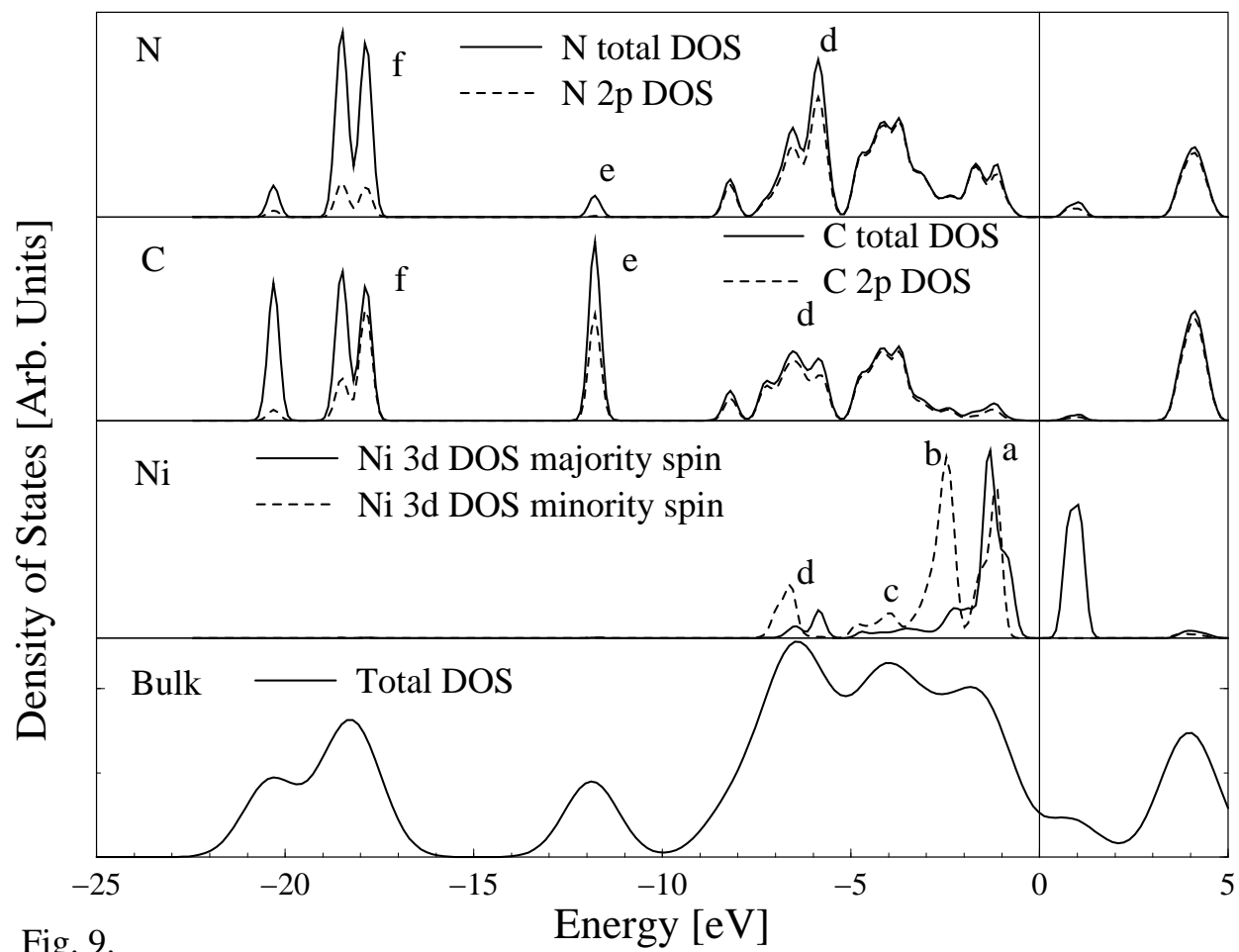


Fig. 9.

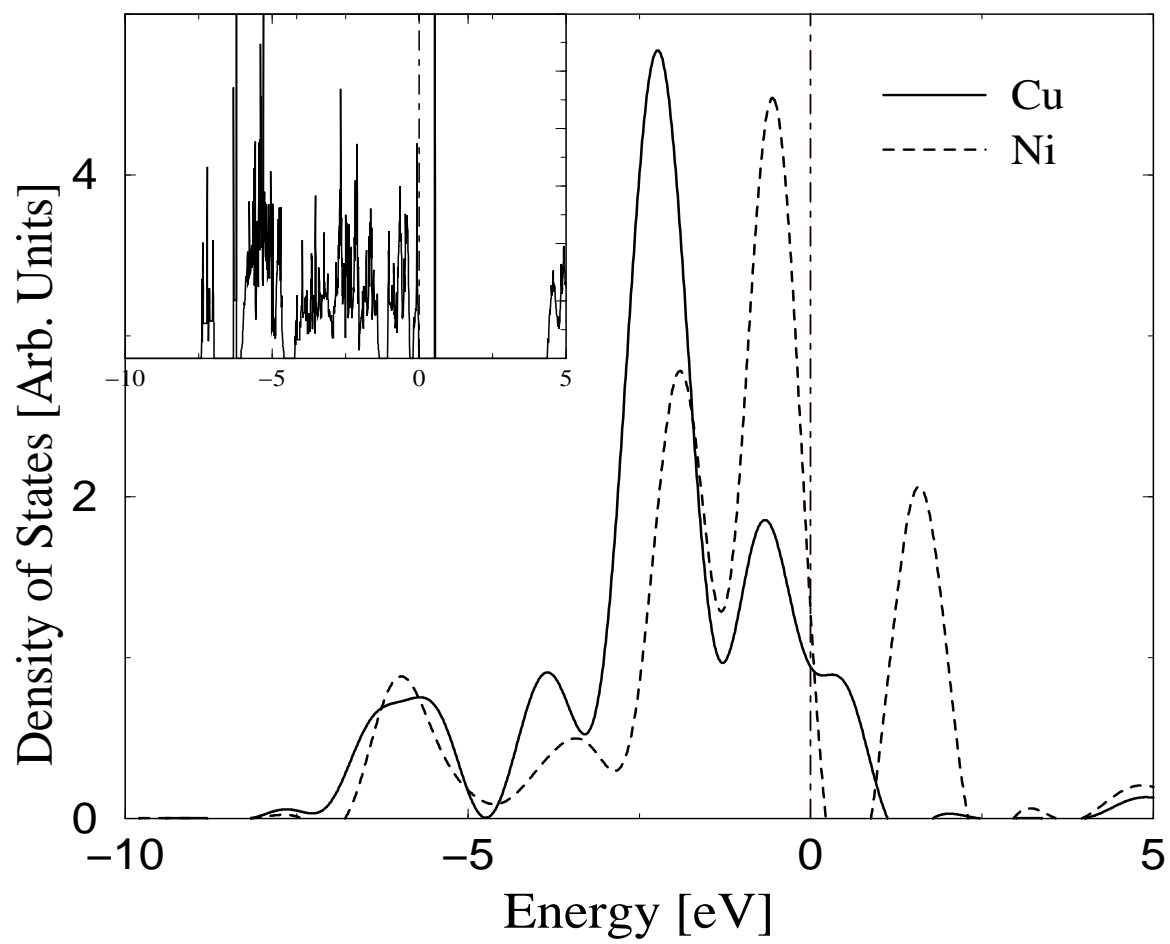


Fig.10.

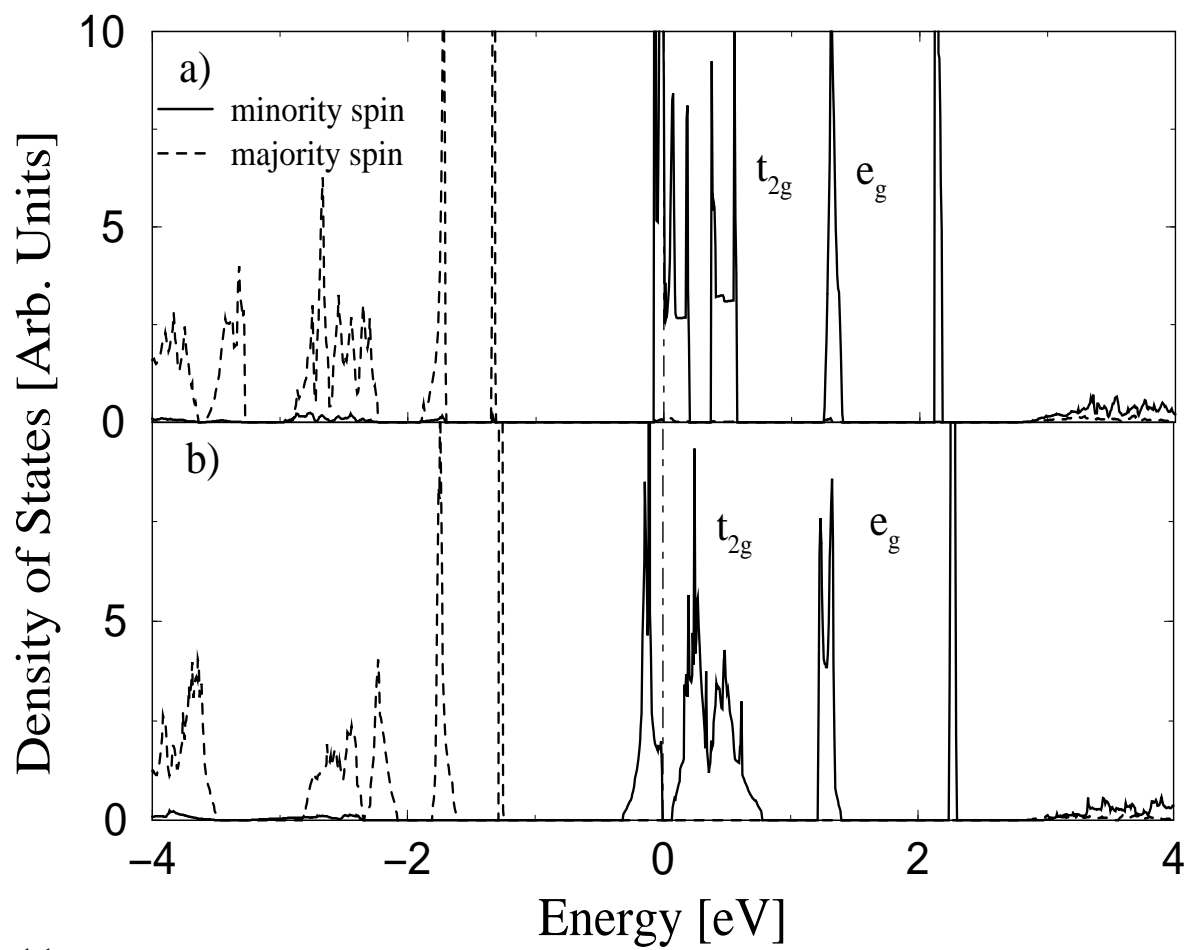


Fig.11.